Synthesis of Strong Light Scattering Absorber of TiO₂−CMK-3/Ag for Photocatalytic Water Splitting under Visible Light Irradiation

Wei Hsuan Hung,*,[†] Sz Nian Lai,[†] and An Ya Lo[‡]

[†]Department of Materials Science and Engineering, Feng-Chia University, Taichung 407, Taiwan
[‡]Department of Chemical and Materials Engineering, National Chin-Yi University of Technology, Taiping 411, Taiwan

S *Supporting Information*

ABSTRACT: The enhanced water splitting photocurrent has been observed through plasmonic mesoporous composite electrode TiO₂−CMK-3/Ag under visible light irradiation. Strong light absorption achieved from the integrations of ordered mesoporous carbon (CMK-3) and silver plasmonic nanoparticles (NPs) layer in the TiO₂, which significantly increased the effective optical depth of TiO₂−CMK-3/Ag photoelectrode. The carbon-based CMK-3 also increased the surface wetting behavior and conductivity of the photoelectrodes, which resulted in a higher ion exchange rate and faster electron transport. The synthesis of high crystalline TiO₂−CMK-3/Ag composite photocatalyst was verified by X-ray diffraction (XRD) and scanning electron microscopy (SEM). Pronounced enhancement of light absorption of TiO₂−CMK-3/Ag photoelectrode was confirmed by UV/vis spectrophotometers. Two orders of magnitude of the enhanced water splitting photocurrent were obtained in the TiO₂−CMK-3/Ag composite photoelectrode with respect to TiO₂ only. Finally, spatially resolved mapping photocurrents were also demonstrated in this study.

KEYWORDS: photocatalytic water splitting, titanium dioxide, mesoporous carbon, plasmonic
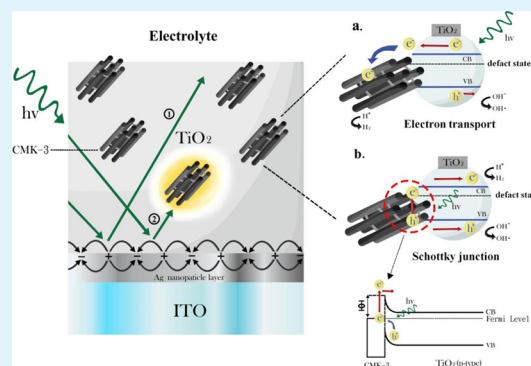
INTRODUCTION

How to improve effectively solar energy conversion to fuel and electricity has been an indispensable topic for decades. The conversion of solar energy into hydrogen energy through photocatalytic water splitting is one of the most important keys to achieve the goal of clean and renewable energy. Many semiconductor metal oxides have been investigated for the water splitting process.[1−5] Titanium dioxide (TiO₂) is one of the most promising materials for photogeneration of hydrogen from water due to its low cost, absence of toxicity and chemical stability.[6−8] However, the mismatch of the optical band gap with the entire solar spectrum constrains the solar photon absorption down to ∼4%.[9] To address this limitation and improve solar conversion efficiency, many efforts have been focused on the development of high surface area nanostructures and the modification of their optical absorption band edge through an elemental doping procedure.[10−12] A high surface area of TiO₂ nanostructures increases the semiconductor/electrolyte interface and reduces diffusion length for minority carriers, which are predicted to be more efficient in charge separation and transport;[13−17] however, it is really difficult to obtain a robust nanostructure, which can prevent the collapse and corrosion of the nanostructure due to the disturbance of acids or bases electrolyte. Likewise, a number of elements (e.g., N, C, transition metals, etc.) have been extensively investigated as dopants for TiO₂ materials in order to extend the absorption

edge to visible light.[18−20] These efforts resulted in slight improvements of the visible light photon absorption.

Increasing the effective optical depth to minimize the amount of materials required to absorb light is one research direction to achieve higher solar energy conversion. The plasmon resonant metal nanoparticle is another promising candidate, which has received much attention, due to a wide range of controllable light absorption.[21−23] Strong light coupling, scattering and intensive near fields are the unique characteristics of these plamonic NPs under the plasmon resonance.[24−28] Many applications have been reported by exploiting these plamonic NPs, including applications of surface enhanced Raman spectroscopy (SERS), solar cells, medicine and photocatalytic chemistry.[27,29−35]

In this study, we proposed a strong light absorption composite photocatalyst TiO₂−CMK-3/Ag to enhance effectively the performance of photocatalytic water splitting under visible light irradiation. The concept of the plasmonic TiO₂−CMK-3/Ag composite photoelectrode is presented in Figure 1. There are three possible enhanced schemes we adopted in our plasmonic cocatalyst photoelectrode to improve the water-splitting process. Scheme 1: the plasmon resonance effect from the underneath silver nanoparticles layer is responsible for
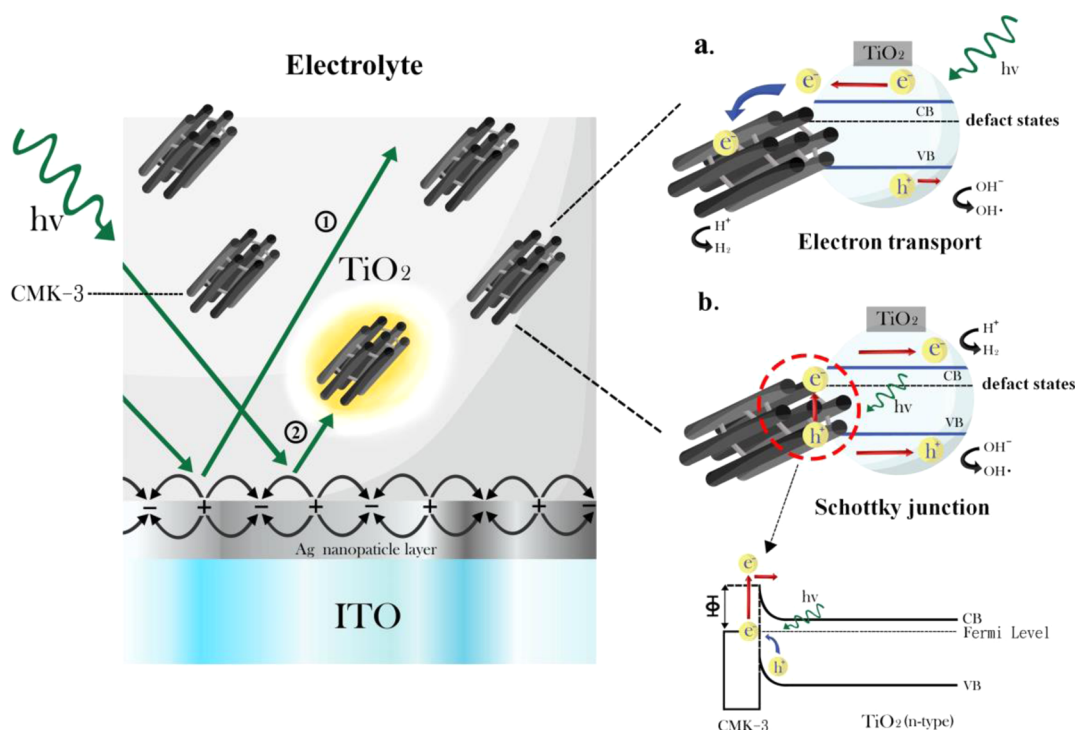
Figure 1. Concept of the plasmonic TiO$_2$–CMK-3/Ag composite photoelectrode and enhanced mechanisms of (a) electron transport and (b) Schottky junction.

creations of a strong light scattering and intensive near fields, which substantially increase the effective absorption depth in the materials. Furthermore, besides the near field and enhanced light absorption during the Plasmon resonance, the discovery of hot electron from plasmon decay process further exploited the utilization of plasmonic NPs, which open a new pathway for many chemical reactions as well.[36−39] Scheme 2: use of high conductive CMK-3 improves the electron transport within the TiO$_2$ matrix to the cathode shown Figure 1a.[40,41] Scheme 3: Schottky junction formation at the interface of TiO$_2$ and CMK-3 enhances the charge separation rate and reduces the exciton recombination.[42−44] In addition, light absorption can be further increased because of the black-body-like property of CMK-3. Moreover, CMK-3 also provides not only a higher reaction surface but also its straight and short mesochannels served as a highway for the faster and deeper transport of electrolyte ions at the surface of photoelecrodes. Briefly, a significantly enhanced water splitting photocurrent is observed in the TiO$_2$–CMK-3/Ag photoelectrode with respect to TiO$_2$ only. The mechanism of photocurrent improvement is investigated by using different structure configurations photoelectro-des.[41,45,46] Spatially resolved photocurrent maps are performed to study the potential production of the large-area fabrication.

■ EXPERIMENTAL SECTION

Titanium dioxide (TiO$_2$) was produced using the standard sol−gel process.[47,48] 20 mL of n-propyl alcohol and 5 mL of titanium(IV) ethoxide (33−35% TiO$_2$, Acros) are added to the beaker with a magnet stirring (1000 rpm) in an ice bath for 12 h. The SBA-15 mesoporous silica template for CMK-3, which was synthesized by using tetraethyl orthosilicate (TEOS) as a precursor and Pluronic P123 (Poly(ethylene glycol)-*block*-poly(ethylene glycol)-*block*-poly-(ethylene glycol)-*block*) copolymer as a surfactant.[49,50] The prepara-tion of ordered mesoporous carbon CMK-3 followed the similar nanocasting procedures reported earlier by using sucrose as the carbon

source.[51−55] Carbonization was completed by pyrolysis of the sample at temperatures of up to 800 °C for 3 h in the argon atmosphere. The carbon−silica composite was leached with 1 wt % HF at room temperature, to remove the silica template. Subsequently, TiO$_2$–CMK-3 colloidal solution was synthesized by adding CMK-3 powder into the TiO$_2$ sol−gel solution. The plasmonic layer of Ag NPs was prepared by a simple chemical reduction. 0.02 g of sliver acstylacetonate (Ag(acac); 98%, Acros) precursor was dissolved in 25 mL of deionized water, and the solution was placed in an ITO substrate for 24 h to form the deposition of the silver nanoparticle layer. Finally, the TiO$_2$–CMK-3/Ag photoelectrode was produced by using a spin-coating method followed by the sintering process at 450 °C for 3 h in nitrogen ambient. Besides the mixed TiO$_2$–CMK-3 structure configuration, we also fabricated the layer type photo-electrode CMK-3/TiO$_2$ by standard spin-coating process for the investigation of enhanced mechanism. Finally, the TiO$_2$–CMK-3/Ag photoelectrode was fabricated by using a spin-coating method followed by the sintering process at 450 °C for 3 h. Again, morphology and microstructure of the samples were investigated using a high resolution transmission electron microscopy (TEM) and field emission scanning electron microscopy (SEM). The ordered arrangement of the CMK-3 carbon and SBA-15 silica was examined by X-ray diffraction (XRD) patterns. UV−visible spectrometry (UV−vis) was employed to characterize the plasmon resonance wavelength of the different photoelectrodes. The specific surface areas were calculated by the Brunauer−Emmett−Teller (BET) method, and the pore size distributions were calculated from an adsorption branch of the isotherm by the Barrett−Joyner−Halenda (BJH) model. Finally, the photocatalytic reaction was measured in 1 M NaOH solution by using three terminal potentiostat at room temperature operation under 532 nm laser irradiation with 1 mm diameter spot size.

■ RESULTS AND DISCUSSIONS

Transmission electron microscopy has been used to study the quality of mesostructured CMK-3, which exhibited a uniform array of mesopores with a long-range order shown in Figure 2a. Energy-dispersive X-ray spectroscopy (EDX) mapping shown
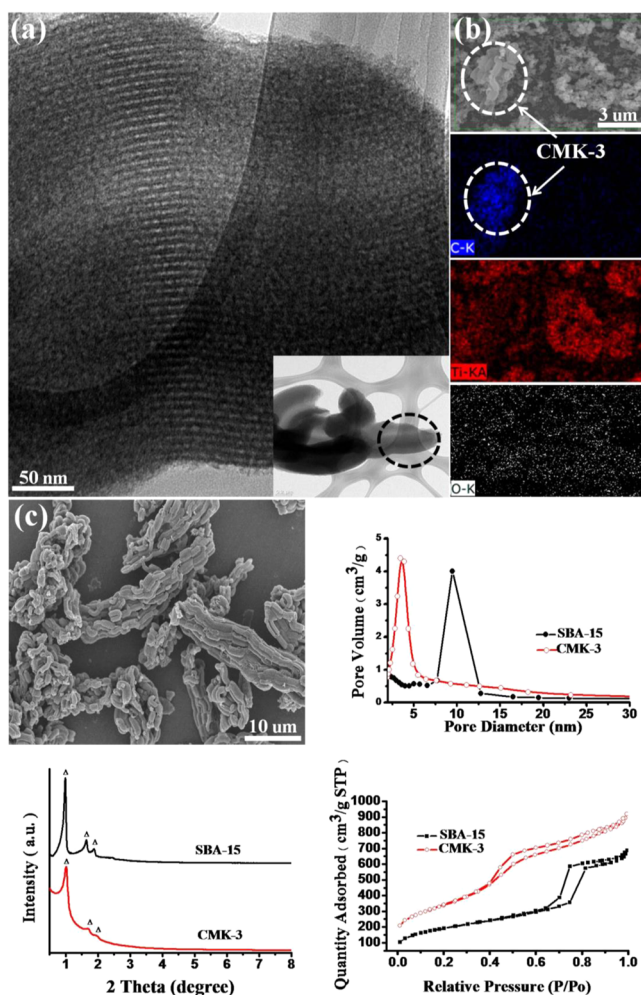
Figure 2. (a) High magnification TEM images of CMK-3. (b) SEM image and corresponding EDX elemental mappings of C, Ti and O of TiO$_2$−CMK-3. (c) Characterization of CMK-3 and corresponding SBA-15 template.

in Figure 2b provides clear information about the C, Ti and O distribution of the TiO$_2$−CMK-3 matrix and further confirms the embedding characteristics of mesoporous CMK-3. Further characterization of CMK-3 has been presented in Figure 2c. The XRD patterns indicated well-ordered mesoporous structures of CMK-3 and corresponding SBA-15 samples, as revealed by the characteristic diffraction peaks at small 2θ angles. All exhibit three peaks in the range 2θ angles of 0.8° to 2.5°, which can be indexed to the (100), (110) and (200) reflections of the hexagonal space group (*P6mm*). Furthermore, the N$_2$ adsorption/desorption isotherms (77 K) for SBA-15, and CMK-3, delivered a common type-IV isotherm with a broad hysteresis loop, which are typical characteristics of capillary condensation in mesoporous channels. According to the pronounced step showed in the adsorption curve, near a 0.45 value of P/P_0, implied the presence of uniform framework-confined (primary) mesoporous. Also, the CMK-3 carbon exhibited a high specific surface of 1500 m^2/g. The average pore diameter is calculated with BJH method showing an approximate value of 3 nm. In addition, the more characterization of different structural TiO$_2$−CMK-3/Ag, TiO$_2$−CMK-3, CMK-3/TiO$_2$ and the layer of silver NPs has been provided (see Figures S1−S4 in the Supporting Information).

Figure 3 shows the absorption spectra of different photoelectrodes. TiO$_2$ showed the normal absorption band edge at
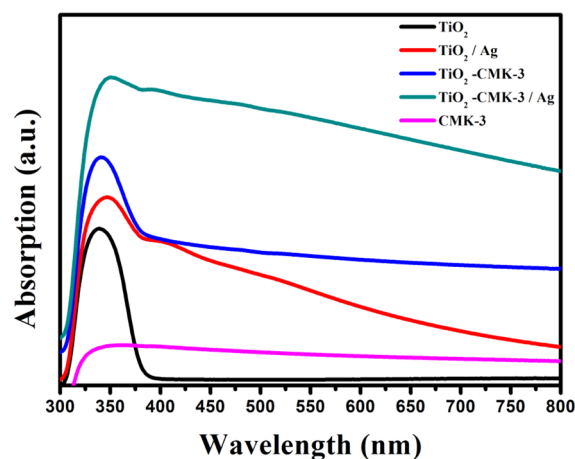

Figure 3. Absorption spectra of different photoelectrode configurations.

390 nm. With the incorporation of silver plasmonic layer, TiO$_2$/Ag exhibited stronger photon absorption owing to the plasmonic boost from the underneath sliver nanoparticles. A small bump of absorption peak appeared at 410 nm was also observed, which is consistent with the typical plasmon resonant absorption peak of Ag nanoparticles. The sample of pure CMK-3, black-body-like materials, exhibited a wide range of wavelength absorption from 350 to 800 nm. When integrating the CMK-3, this raised the TiO$_2$−CMK-3 entire absorption spectrum above both of TiO$_2$ and TiO$_2$/Ag. Ultimately, the highest light absorption was obtained in the TiO$_2$−CMK-3/Ag composite photoelectrode due to the severe multiple light absorption and scattering processes within the Ag NPs and CMK-3.

In addition, the improvement of the wettability of TiO$_2$−CMK-3 was confirmed by the measurement of the contact angle of a water drop on both TiO$_2$−CMK-3 and TiO$_2$ only surfaces. Even though the surface of TiO$_2$ is well-known for its hydrophilic property, with the integration of CMK-3, the contact angle of a water drop on the surface of TiO$_2$−CMK-3 electrode can be still slightly reduced from 24.45° to 22.06°, shown in Figure 4a. The result implies that the high porosity of CMK-3 provide an additional transmission channel to improve ionic electrolyte transport at the surface of the photoelectrodes, reducing the accumulation of byproducts during water splitting reaction. Besides the measurement of the contact angle of a water drop, the analysis of the sheet resistances was performed by four-point probe measurements on samples of TiO$_2$ and TiO$_2$−CMK-3/Ag. According to the average result of 10 points with standard deviation less than 3% error, the sheet resistance of TiO$_2$−CMK-3/Ag photoelectrode is approximately 6 times smaller than that of TiO$_2$ due to the combination of the CMK-3 and Ag NPs. It suggests that the conduction of carriers can be more effectively in the TiO$_2$−CMK-3/Ag photoelectrode.

The photocurrent responses were measured by a traditional three-electrode measurement method with prepared samples, a Ag/AgCl electrode, a graphite rod functioning as the working, reference and counter electrodes, respectively. Four different structure configuration photoelectrodes were performed under a constant applied voltage of 0.05 V, including the TiO$_2$, TiO$_2$−CMK-3 (mixed), CMK-3/TiO$_2$ (layers), TiO$_2$/Ag and TiO$_2$−
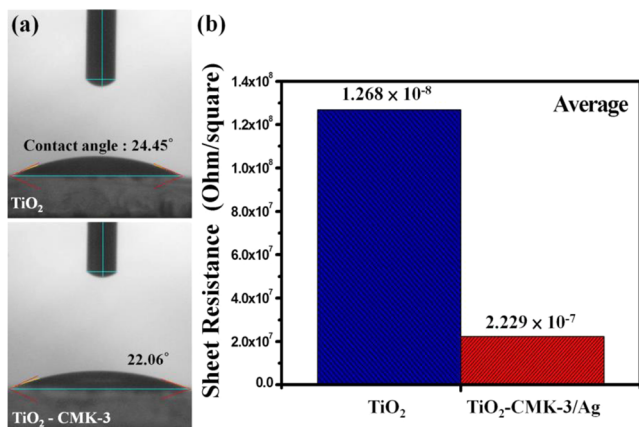
Figure 4. (a) Water contact angle of TiO_2 only and TiO_2–CMK-3. (b) Four-point probe measurements in thin film chip resistors.

CMK-3/Ag photoelectrodes. Figure 5a shows the photocurrent response of these different photoelectrodes under the 532 nm laser irradiation with a power of 500 mW. During the 532 nm laser excitation, TiO_2 photoelectrode presented no obvious photocurrent generation due to its wide band gap (3.2 eV), limiting the effective absorption of low energy photons. With the incorporation of CMK-3, both TiO_2–CMK-3 (mixed) and CMK-3/TiO_2 (layers) exhibited higher photocurrent responses than that of TiO_2 only. The enhancement of photocurrent is attributed to the absorption improvement from CMK-3, which is consistent with the results observed in the previous absorption spectrum. Interestingly, different structure configuration of CMK-3/TiO_2 (layers) showed relatively lower photocurrent as compared to TiO_2–CMK-3 (mixed), resulting from the reduction of reaction sites of TiO_2 as CMK-3 on top of the reaction surface. With the integration of plasmonic sliver NPs, the improvement of the incident photon absorption has been reflected on the performance of photocurrent response of

TiO_2/Ag, which exhibited second highest photocurrent in these samples. However, the highest photocurrent response obtained at the TiO_2–CMK-3/Ag photoelectrode, which showed two times higher photocurrent than that of TiO_2–CMK-3. This observation suggests that existence of plasmonic silver nanoparticles can significantly amplify the effective exciton generation due to the plasmon resonant effects from the silver NPs. This argument is also supported by our absorption spectrum, which displayed the highest photon absorption in the sample of TiO_2–CMK-3/Ag. However, all of the photocurrent responses in Figure 5a were measured under a small applied voltage of 0.05 V, and additional photocurrent responses at higher applied voltages are provided (see Figure S5 in the Supporting Information). Figure 5b delivers the results of the power dependence study of TiO_2–CMK-3/Ag, which indicates a linear relation between the laser power and water-splitting photocurrent in the range from 100 to 500 mW. For further comparison, the power dependence study of the TiO_2–CMK-3 photoelectrode has also been plotted together in Figure 5c, which shows a similar minimum threshold laser power but with a smaller slope for the increase of photocurrent. Furthermore, prolonged photocurrent measurements were performed to examine the stability of the TiO_2–CMK-3/Ag photoelectrode, which are provided in the (see Figure S6 in the Supporting Information).

The investigation of the charge transfer of photogenerated electron and hole pairs can be achieved by the photoluminescence (PL) emission spectrum, which its signal indicates the recombination of free charge carriers. Figure 6a shows the PL spectra of different samples with the excitation wavelength at 263 nm (4.71 eV). On the basis of the PL results, the intensity of emission peaks at approximately 525 nm decreased with the existence of CMK-3 or sliver NPs and the weakest emission signal occurred at the sample of TiO_2–CMK-3/Ag. These results suggested that the recombination of charge carriers was significantly reduced with integration of silver NPs and CMK-3. This suppression of charge recombination also
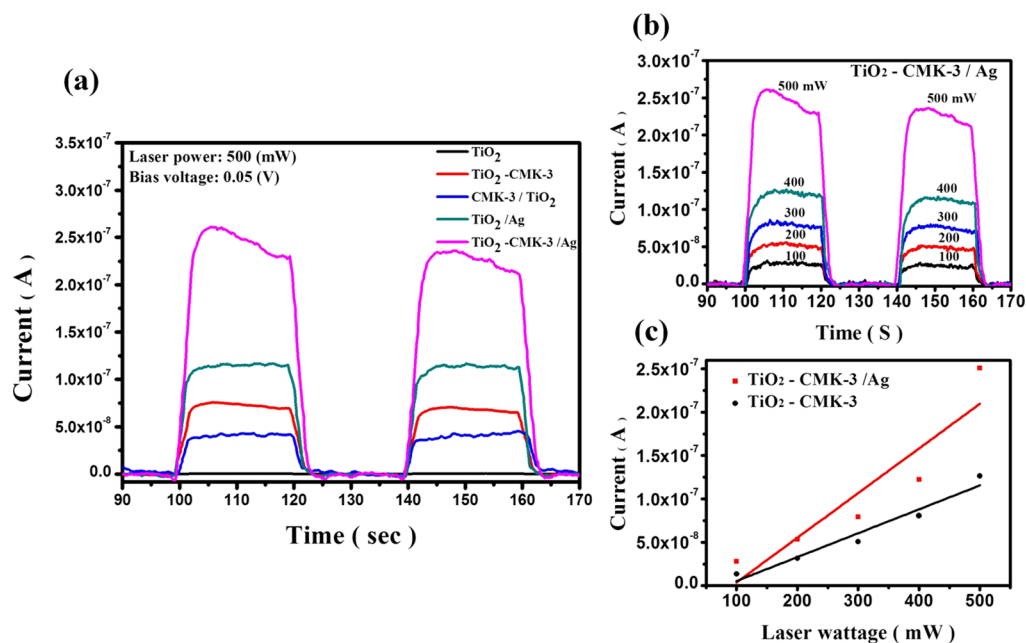

Figure 5. (a) Photocurrent response of different photoelectrodes. (b) Power depend study of TiO_2–CMK-3/Ag. (c) Photocurrent response comparison of TiO_2–CMK-3 and with TiO_2–CMK-3/Ag photoelectrodes under different laser power irradiations.
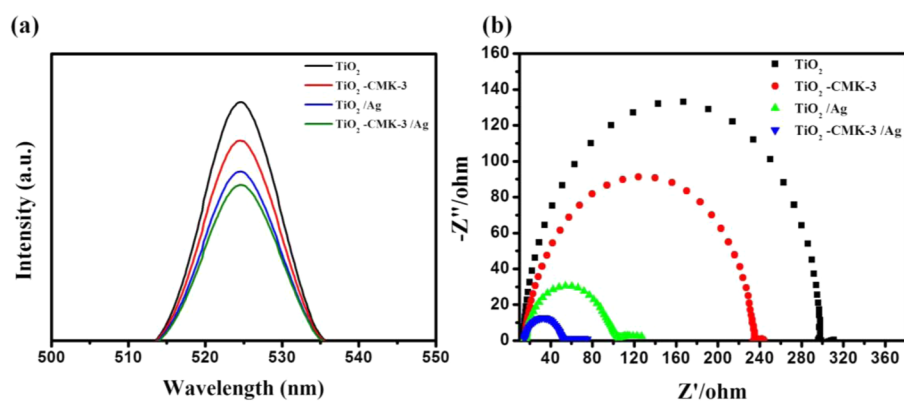
Figure 6. (a) Photoluminescence spectra of the TiO_2, TiO_2−CMK-3, TiO_2/Ag and TiO_2−CMK-3/Ag photoelectrodes under 263 nm UV excitation. (b) Nyquist plots of different photoelectrodes.
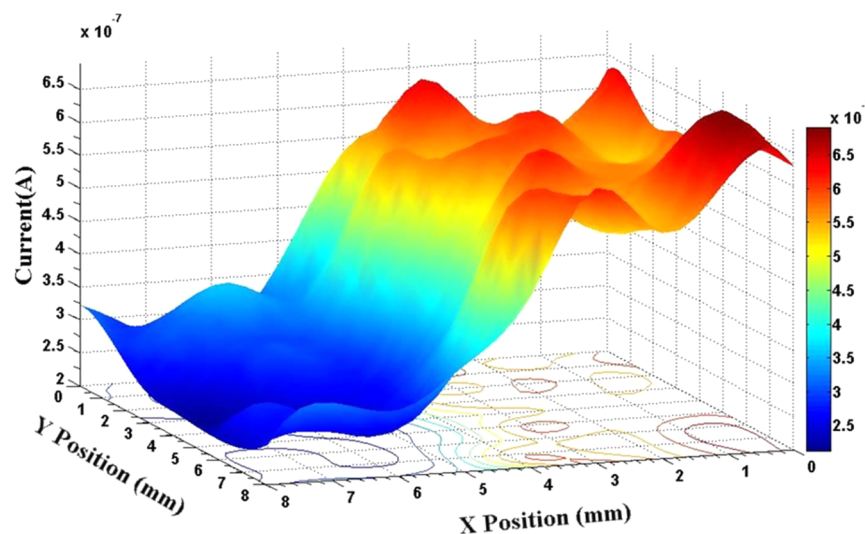

Figure 7. Spatial distribution photocurrent of a step design structure photoelectrode.

proved the possible formation of Schottky junction at the interface of TiO_2 and CMK-3 as the explanation in Figure 1. In addition, to understand the charge transfer at the interface of photoeletrode and electrolyte, we conducted the measurement of electrochemical impedance spectroscopy (EIS) as well. Figure 6b shows Nyquist plot of all the four tested photoelectrodes under 532 nm laser irradiation. Electrochemical impedance spectra were recorded at DC potential of 1.23 V vs RHE and an AC potential frequency range of 100 000−0.01 Hz. The diameters of the semicircles in Nyquist plot indicate the charge transfer resistance of samples. Similarly, the charge transfer resistance ofTiO$_2$ was improved with the integration of either silver NPs or CMK-3. The smallest arch diameter was observed in the sample of TiO_2−CMK-3/Ag, which suggested efficient charge transfer from the surface of TiO_2−CMK-3 matrix to the electrolyte. This result is in agreement with the observations of the outcomes of photocurrent responses and the four-point probe measurement.

Finally, the spatial distribution of water splitting photocurrent has also been examined by a step design structure in the photoelectrode. The concept of the step design in the photoelectrode is that, instead of covering the full area, plasmonic silver layer only covers half of photoelectrode underneath the TiO_2−CMK-3 layer. Spatially resolved mapping photocurrents were measured by rastering the 532 nm laser

focus across both plasmon enhanced and nonplasmon enhanced region. With a higher laser power of 800 mW, more significant photocurrent gap was displayed between the enhanced and nonenhanced area shown in Figure 7, which we primitively expected from this step design photoelectrode. The top of the stair exhibited an enhanced photocurrent in an area of 3 × 8 mm due to the existence of silver plasmonic layer. Photocurrent distribution is not perfectly uniform in the whole enhanced area, which can be attributed to the arbitrary shape of plasmonic silver nanoparticles. However, this entire plasmon enhanced area still shows more than 4 times enhanced photocurrent with respect to that in bottom of the stair (TiO_2−CMK-3 only). This demonstration proves a potential application of using the plasmonic TiO_2−CMK-3/Ag photoelectrode for improving solar water splitting in the large scale area.

■ CONCLUSIONS

This study has successfully achieved the synthesis of a TiO_2−CMK-3/Ag composite photocatalyst for the enhancement of the photocurrent responses in water splitting process under visible light irradiation. In our design, the combination of mesoporous CMK-3 and plasmonic silver layer constituted a perfect resonance circumstance for the internal light absorption from taking advantage of the plasmon resonance effects and the

formation of Schottky junctions. The mechanism of photo-current improvement has been investigated by using different structure configurations photoelectrodes. In addition, the improvement of the wettability and the lower sheet resistances were observed in the TiO_2−CMK-3/Ag, benefiting the ionic electrolyte transport and carrier conduction at the surface of the photoelectrodes. Finally, we also performed the measurement of the spatial distribution of water splitting photocurrent in the TiO_2−CMK-3/Ag photoelectrode for the demonstration of solar water splitting over the large scale area.

■ ASSOCIATED CONTENT

Ⓢ Supporting Information

SEM, TEM and XRD images of composite materials; EDS spectra of composite photocatalyst flims and the photocurrent response of TiO_2−CMK-3/Ag at high bias. This material is available free of charge via the Internet at http://pubs.acs.org.

■ AUTHOR INFORMATION

Corresponding Author
*W. H. Hung. E-mail: whung@fcu.edu.tw.

Notes
The authors declare no competing financial interest.

■ ACKNOWLEDGMENTS

■ REFERENCES

(1) Yang, X. Y.; Wolcott, A.; Wang, G. M.; Sobo, A.; Fitzmorris, R. C.; Qian, F.; Zhang, J. Z.; Li, Y. Nitrogen-Doped ZnO Nanowire Arrays for Photoelectrochemical Water Splitting. *Nano Lett.* **2009**, *9*, 2331−2336.

(2) Sivula, K.; Le Formal, F.; Gratzel, M. Solar Water Splitting: Progress Using Hematite (α-Fe_2O_3) Photoelectrodes. *ChemSusChem* **2011**, *4*, 432−449.

(3) Tacca, A.; Meda, L.; Marra, G.; Savoini, A.; Caramori, S.; Cristino, V.; Bignozzi, C. A.; Pedro, V. G.; Boix, P. P.; Gimenez, S.; Bisquert, J. Photoanodes Based on Nanostructured WO_3 for Water Splitting. *ChemPhysChem* **2012**, *13*, 3025−3034.

(4) Manikandan, M.; Tanabe, T.; Li, P.; Ueda, S.; Ramesh, G. V.; Kodiyath, R.; Wang, J. J.; Hara, T.; Dakshanamoorthy, A.; Ishihara, S.; Ariga, K.; Ye, J. H.; Umezawa, N.; Abe, H. Photocatalytic Water Splitting under Visible Light by Mixed-Valence Sn_3O_4. *ACS Appl. Mater. Interfaces* **2014**, *6*, 3790−3793.

(5) Ng, C.; Ng, Y. H.; Iwase, A.; Amal, R. Influence of Annealing Temperature of WO_3 in Photoelectrochemical Conversion and Energy Storage for Water Splitting. *ACS Appl. Mater. Interfaces* **2013**, *5*, 5269−5275.

(6) Fujishima, A.; Zhang, X. T. Titanium Dioxide Photocatalysis: Present Situation and Future Approaches. *C. R. Chim.* **2006**, *9*, 750−760.

(7) Hashimoto, K.; Irie, H.; Fujishima, A. TiO_2 Photocatalysis: A Historical Overview and Future Prospects. *Jpn. J. Appl. Phys.* **2005**, *44*, 8269−8285.

(8) Zhang, X.; Liu, Y.; Kang, Z. H. 3D Branched ZnO Nanowire Arrays Decorated with Plasmonic Au Nanoparticles for High-Performance Photoelectrochemical Water Splitting. *ACS Appl. Mater. Interfaces* **2014**, *6*, 4480−4489.

(9) Tabaei, H. S. M.; Kazemeini, M.; Fattahi, M. Preparation and Characterization of Visible Light Sensitive Nano Titanium Dioxide Photocatalyst. *Sci. Iran.* **2012**, *19*, 1626−1631.

(10) Pan, M. M.; Huang, N.; Zhao, X. Z.; Fu, J.; Zhong, X. L. Enhanced Efficiency of Dye-Sensitized Solar Cell by High Surface Area Anatase-TiO_2-Modified P25 Paste. *J. Nanomater.* **2013**, 1−6.

(11) Chen, D. H.; Huang, F. Z.; Cheng, Y. B.; Caruso, R. A. Mesoporous Anatase TiO_2 Beads with High Surface Areas and Controllable Pore Sizes: A Superior Candidate for High-Performance Dye-Sensitized Solar Cells. *Adv. Mater.* **2009**, *21*, 2206−2210.

(12) Yang, G. D.; Jiang, Z.; Shi, H. H.; Xiao, T. C.; Yan, Z. F. Preparation of Highly Visible-Light Active N-Doped TiO_2 Photocatalyst. *J. Mater. Chem.* **2010**, *20*, 5301−5309.

(13) Chen, B.; Doucette, G.; Priya, S. Improved Performance of Flexible Dye-Sensitized Solar Cells Based on Hierarchical TiO_2 Nanostructures with High Surface Area. *RSC Adv.* **2013**, *3*, 24560−24566.

(14) Pan, X.; Zhao, Y.; Fan, Z. Y. TiO_2 Nanostructures by Electrochemical Anodization for Dye-Sensitized Solar Cells. *Nanosci. Nanotechnol. Lett.* **2012**, *4*, 463−470.

(15) Guo, L. M.; Hagiwara, H.; Ida, S.; Daio, T.; Ishihara, T. One-Pot Soft-Templating Method to Synthesize Crystalline Mesoporous Tantalum Oxide and Its Photocatalytic Activity for Overall Water Splitting. *ACS Appl. Mater. Interfaces* **2013**, *5*, 11080−11086.

(16) Regonini, D.; Teloeken, A. C.; Alves, A. K.; Berutti, F. A.; Gajda-Schrantz, K.; Bergmann, C. P.; Graule, T.; Clemens, F. Electrospun TiO_2 Fiber Composite Photoelectrodes for Water Splitting. *ACS Appl. Mater. Interfaces* **2013**, *5*, 11747−11755.

(17) Bwana, N. N. Effects of the Morphology of the Electrode Nanostructures on the Performance of Dye-Sensitized Solar Cells. *Nano Res.* **2008**, *1*, 483−489.

(18) Li, H. Y.; Wang, D. J.; Fan, H. M.; Wang, P.; Jiang, T. F.; Xie, T. F. Synthesis of Highly Efficient C-Doped TiO_2 Photocatalyst and Its Photo-generated Charge-Transfer Properties. *J. Colloid Interface Sci.* **2011**, *354*, 175−180.

(19) Liu, B.; Chen, H. M.; Liu, C.; Andrews, S. C.; Hahn, C.; Yang, P. D. Large-Scale Synthesis of Transition-Metal-Doped TiO_2 Nanowires with Controllable Overpotential. *J. Am. Chem. Soc.* **2013**, *135*, 9995−9998.

(20) Wang, H.; Quan, X.; Yu, H. T.; Chen, S. Fabrication of a TiO_2/Carbon Nanowall Heterojunction and Its Photocatalytic Ability. *Carbon* **2008**, *46*, 1126−1132.

(21) Xu, M. F.; Zhu, X. Z.; Shi, X. B.; Liang, J.; Jin, Y.; Wang, Z. K.; Liao, L. S. Plasmon Resonance Enhanced Optical Absorption in Inverted Polymer/Fullerene Solar Cells with Metal Nanoparticle-Doped Solution-Processable TiO_2 Layer. *ACS Appl. Mater. Interfaces* **2013**, *5*, 2935−2942.

(22) Catchpole, K. R.; Polman, A. Plasmonic Solar Cells. *Opt. Express* **2008**, *16*, 21793−21800.

(23) Pavaskar, P.; Hsu, I. K.; Theiss, J.; Hung, W. H.; Cronin, S. B. A Microscopic Study of Strongly Plasmonic Au and Ag Island Thin Films. *J. Appl. Phys.* **2013**, *113*, 034302-1−034302-6.

(24) Noguez, C. Surface Plasmons on Metal Nanoparticles: The Influence of Shape and Physical Environment. *J. Phys. Chem. C* **2007**, *111*, 3806−3819.

(25) Giannini, V.; Fernandez-Dominguez, A. I.; Heck, S. C.; Maier, S. A. Plasmonic Nanoantennas: Fundamentals and Their Use in Controlling the Radiative Properties of Nanoemitters. *Chem. Rev.* **2011**, *111*, 3888−3912.

(26) Hou, W. B.; Liu, Z. W.; Pavaskar, P.; Hung, W. H.; Cronin, S. B. Plasmonic Enhancement of Photocatalytic Decomposition of Methyl Orange under Visible Light. *J. Catal.* **2011**, *277*, 149−153.

(27) Hou, W. B.; Hung, W. H.; Pavaskar, P.; Goeppert, A.; Aykol, M.; Cronin, S. B. Photocatalytic Conversion of CO_2 to Hydrocarbon Fuels via Plasmon-Enhanced Absorption and Metallic Interband Transitions. *ACS Catal.* **2011**, *1*, 929−936.

(28) Zhan, Z. Y.; An, J. N.; Zhang, H. C.; Hansen, R. V.; Zheng, L. X. Three-Dimensional Plasmonic Photoanodes Based on Au-Embedded

TiO$_2$ Structures for Enhanced Visible-Light Water Splitting. *ACS Appl. Mater. Interfaces* **2014**, *6*, 1139−1144.

(29) Kumar, G. V. P. Plasmonic Nano-architectures for Surface Enhanced Raman Scattering: A Review. *J. Nanophotonics* **2012**, *6*, 064503-1−064503-20.

(30) Su, Y. H.; Ke, Y. F.; Cai, S. L.; Yao, Q. Y. Surface Plasmon Resonance of Layer-by-Layer Gold Nanoparticles Induced Photoelectric Current in Environmentally-Friendly Plasmon-Sensitized Solar Cell. *Light: Sci. Appl.* **2012**, *1*, 1−5.

(31) Liao, H. W.; Nehl, C. L.; Hafner, J. H. Biomedical Applications of Plasmon Resonant Metal Nanoparticles. *Nanomedicine* **2006**, *1*, 201−208.

(32) Liu, Z. W.; Hou, W. B.; Pavaskar, P.; Aykol, M.; Cronin, S. B. Plasmon Resonant Enhancement of Photocatalytic Water Splitting Under Visible Illumination. *Nano Lett.* **2011**, *11*, 1111−1116.

(33) Liu, Z. W.; Hung, W. H.; Aykol, M.; Valley, D.; Cronin, S. B. Optical Manipulation of Plasmonic Nanoparticles, Bubble Formation and Patterning of SERS Aggregates. *Nanotechnology* **2010**, *21*, 1−5.

(34) Sun, Y. Q.; Chemelewski, W. D.; Berglund, S. P.; Li, C.; He, H. C.; Shi, G. Q.; Mullins, C. B. Antimony-Doped Tin Oxide Nanorods as a Transparent Conducting Electrode for Enhancing Photoelectrochemical Oxidation of Water by Hematite. *ACS Appl. Mater. Interfaces* **2014**, *6*, 5494−5499.

(35) Liu, L. P.; Wang, G. M.; Li, Y.; Li, Y. D.; Zhang, J. Z. CdSe Quantum Dot-Sensitized Au/TiO$_2$ Hybrid Mesoporous Films and Their Enhanced Photoelectrochemical Performance. *Nano Res.* **2011**, *4*, 249−258.

(36) Lee, Y. K.; Lee, J.; Lee, H.; Lee, J. Y.; Park, J. Y. Probing Polarization Modes of Ag Nanowires with Hot Electron Detection on Au/TiO$_2$ Nanodiodes. *Appl. Phys. Lett.* **2013**, *102*, 123112-1−123112-5.

(37) Knight, M. W.; Sobhani, H.; Nordlander, P.; Halas, N. J. Photodetection with Active Optical Antennas. *Science* **2011**, *332*, 702−704.

(38) Fan, W. G.; Jewell, S.; She, Y. Y.; Leung, M. K. H. In Situ Deposition of Ag-Ag2S Hybrid Nanoparticles onto TiO$_2$ Nanotube Arrays towards Fabrication of Photoelectrodes with High Visible Light Photoelectrochemical Properties. *Phys. Chem. Chem. Phys.* **2014**, *16*, 676−680.

(39) Trost, S.; Becker, T.; Zilberberg, K.; Behrendt, A.; Polywka, A.; Heiderhoff, R.; Gorrn, P.; Riedl, T. Plasmonically Sensitized Metal-Oxide Electron Extraction Layers for Organic Solar Cells. *Sci. Rep.* **2015**, *5*, 1−9.

(40) Zhang, B.; Chen, X. D.; Yang, J.; Yu, D. S.; Chen, Y. J.; Wu, D. C.; Fu, R. W.; Zhang, M. Q. Enhanced Photoresponse of CdS/CMK-3 Composite as a Candidate for Light-Harvesting Assembly. *Nanotechnology* **2010**, *21*, 1−7.

(41) Solovyov, L. A.; Shmakov, A. N.; Zaikovskii, V. I.; Joo, S. H.; Ryoo, R. Detailed Structure of The Hexagonally Packed Mesostructured Carbon Material CMK-3. *Carbon* **2002**, *40*, 2477−2481.

(42) Song, J. L.; Yin, Z. Y.; Yang, Z. J.; Amaladass, P.; Wu, S. X.; Ye, J.; Zhao, Y.; Deng, W. Q.; Zhang, H.; Liu, X. W. Enhancement of Photogenerated Electron Transport in Dye-Sensitized Solar Cells with Introduction of a Reduced Graphene Oxide-TiO$_2$ Junction. *Chem.—Eur. J.* **2011**, *17*, 10832−10837.

(43) Woan, K.; Pyrgiotakis, G.; Sigmund, W. Photocatalytic Carbon-Nanotube-TiO$_2$ Composites. *Adv. Mater.* **2009**, *21*, 2233−2239.

(44) Meng, T.; Wang, M.; Jiang, F.; Yu, J.; Hu, Y.; Wu, K. Photocatalytic Property of Ag Modified Nano-TiO$_2$/Carbon Nanotube Composites for NO$_2$ Degradation under Visible Light. *Mater. Res. Innovations* **2014**, *18*, 691−695.

(45) Shilapuram, V.; Ozalp, N.; Oschatz, M.; Borchardt, L.; Kaskel, S. Hydrogen Production from Catalytic Decomposition of Methane over Ordered Mesoporous Carbons (CMK-3) and Carbide-Derived Carbon (DUT-19). *Carbon* **2014**, *67*, 377−389.

(46) Onfroy, T.; Guenneau, F.; Springuel-Huet, M. A.; Gedeon, A. First Evidence of Interconnected Micro and Mesopores in CMK-3 Materials. *Carbon* **2009**, *47*, 2352−2357.

(47) Sugimoto, T.; Zhou, X. P.; Muramatsu, A. Synthesis of Uniform Anatase TiO$_2$ Nanoparticles by Gel-Sol Method 3. Formation Process and Size Control. *J. Colloid Interface Sci.* **2003**, *259*, 43−52.

(48) Sonawane, R. S.; Dongare, M. K. Sol-Gel Synthesis of Au/TiO$_2$ Thin Films for Photocatalytic Degradation of Phenol in Sunlight. *J. Mol. Catal. A: Chem.* **2006**, *243*, 68−76.

(49) Zhao, D. Y.; Feng, J. L.; Huo, Q. S.; Melosh, N.; Fredrickson, G. H.; Chmelka, B. F.; Stucky, G. D. Triblock Copolymer Syntheses of Mesoporous Silica with Periodic 50 to 300 Angstrom Pores. *Science* **1998**, *279*, 548−552.

(50) Zhao, D.; Yang, P.; Melosh, N.; Feng, J.; Chmelka, B. F.; Stucky, G. D. Continuous Mesoporous Silica Films with Highly Ordered Large Pore Structures. *Adv. Mater.* **1998**, *10*, 1380−1385.

(51) Jun, S.; Joo, S. H.; Ryoo, R.; Kruk, M.; Jaroniec, M.; Liu, Z.; Ohsuna, T.; Terasaki, O. Synthesis of New, Nanoporous Carbon with Hexagonally Ordered Mesostructure. *J. Am. Chem. Soc.* **2000**, *122*, 10712−10713.

(52) Dibandjo, P.; Chassagneux, F.; Bois, L.; Sigala, C.; Miele, P. Comparison between SBA-15 Silica and CMK-3 Carbon Nanocasting for Mesoporous Boron Nitride Synthesis. *J. Mater. Chem.* **2005**, *15*, 1917−1923.

(53) Niebrzydowska, P.; Janus, R.; Kustrowski, P.; Jarczewski, S.; Wach, A.; Silvestre-Albero, A. M.; Rodriguez-Reinoso, F. A Simplified Route to The Synthesis of CMK-3 Replica Based on Precipitation Polycondensation of Furfuryl Alcohol in SBA-15 Pore System. *Carbon* **2013**, *64*, 252−261.

(54) Fuertes, A. B. Synthesis of Ordered Nanoporous Carbons of Tunable Mesopore Size by Templating SBA-15 Silica Materials. *Microporous Mesoporous Mater.* **2004**, *67*, 273−281.

(55) Liu, S. H.; Lu, R. F.; Huang, S. J.; Lo, A. Y.; Chien, S. H.; Liu, S. B. Controlled Synthesis of Highly Dispersed Platinum Nanoparticles in Ordered Mesoporous Carbon. *Chem. Commun.* **2006**, 3435−3437.